The International Journal of Advanced Manufacturing Technology (2018) 96:1497–1506
https://doi.org/10.1007/s00170-018-1707-5

ORIGINAL ARTICLE

Impact of shoulder concavity on non-tool-tilt friction stir welding of 5052 aluminum alloy

H. J. Zhang [1,2] · M. Wang [2] · Z. Zhu [2] · X. Zhang [2] · T. Yu [2] · Z. Q. Wu [2]

Received: 2 July 2017 / Accepted: 5 February 2018 / Published online: 13 February 2018

Abstract
In regard to the non-tool-tilt friction stir welding (NTT-FSW) process, the shoulder concavity has significant effects on the control of heat generation and material flow, and thus is an important geometrical feature for the tool design. In this paper, three types of shoulder concavity angles (SCAs), i.e., 0°, 5°, and 10°, were selected to explore the impact of SCA on the NTT-FSW of 5052 aluminum alloy. The results indicate that the increase of SCA lowers the tool axial force, reduces the nugget width, and weakens the band structure in the nugget. A weakening of shoulder thermal effect occurs from 0° to 5° SCA, leading to an improvement of the structure-property of the NTT-FSW joint. Further increasing the SCA to 10° causes the generation of the secondary sliding frictional heat at the interface between the shoulder-driven material and the base material, and thus the shoulder thermal effect does not show a continuous weakening trend as expected but becomes stronger instead, resulting in the deterioration of the microstructure evolution and the degradation of the tensile strength of NTT-FSW joint.

Keywords Non-tool-tilt friction stir welding · Shoulder concavity · Aluminum alloy · Joint performance

1 Introduction

Friction stir welding (FSW) is a solid state joining process especially suitable for the high-quality welding of low-melting-point metals. During FSW, the rotating tool that generally consists of a shoulder and a pin is inserted into the top surface of workpiece and then moves along the welding line. After that, a FSW joint is produced [1, 2]. Traditionally, the tilting of the tool from the normal workpiece against tool travel direction is required to produce a compressive forging force on the weld and thus improve the material stirring and nugget integrity [3, 4]. However, the conventional FSW with tool tilting angle is mainly used to produce linear welds. It has limitations in terms of the generation of nonlinear welds [5, 6]. In order to meet the requirement of the manufacturing of complex structures with nonlinear welds (curved welds or even three-dimensional space welds), the non-tool-tilt FSW (NTT-FSW) process that allows the FSW with zero tool tilting angle has been developed and extensively applied in recent years [3–5].

FSW is a complex thermo-mechanical process. The final performances of the FSW joint are closely related to the tool geometries and welding parameters. Because of this, the tool design is always of prime importance for the investigation of FSW. The tool geometry, especially the shoulder geometry, plays critical roles in generating the frictional heat and regulating the material flow during FSW. Concave shoulder is an important geometry shape of the shoulder end surface for the conventional FSW. It cannot only act as a reservoir for the plastic material, but also enhance the material plastic flow beneath tool shoulder [4]. In fact, the concave shoulder is also available and beneficial for the NTT-FSW process. Compared with the flat shoulder, the concave shoulder provides larger escape volume for the displaced material from the tool pin; thus, it facilitates the reduction of weld flash [7, 8]. Furthermore, in contrast to the conventional FSW, the NTT-FSW process using concave-shouldered tool has been demonstrated to be able to reduce the shoulder thermal effect and improve the joint properties [9].

In the conventional FSW process, the shoulder concavity angle (SCA) is an important parameter for the concave shoulder, which plays decisive roles in both weld formation and

✉ H. J. Zhang
zhanghuijie@sia.cn

[1] School of Materials Science and Engineering, Northeastern University, Shenyang 110819, People's Republic of China

[2] State Key Laboratory of Robotics, Shenyang Institute of Automation Chinese Academy of Sciences, Shenyang 110016, People's Republic of China

joint properties. The influence of SCA on material flow pattern and joint properties for conventional FSW has been reported by several existing literatures [7, 8, 10]. However, very few studies are focused on the effect of SCA on the NTT-FSW until now. Apparently, deep investigation on this topic is required for the tool design and process control of NTT-FSW. Therefore, a 5052 aluminum alloy was friction stir welded at a zero tool tilting angle. The impact of SCA on joint performances, including weld formation, mechanical property, and microstructure evolution, was comprehensively investigated, and the thermo-mechanical effect feature of concave shoulder that determined the joint performances was also explored.

2 Experimental procedure

The base metal (BM) used for this investigation was an 8-mm-thick 5052 aluminum alloy plate in H32 condition, which is a type of Al-Mg series antirust aluminum alloy widely used in planes and automobiles. The chemical compositions and mechanical properties of the BM are listed in Table 1. The dimension of welding samples was 300 mm long by 150 mm wide.

Three types of tool shoulders were utilized in the study. The shoulder surface of one tool was flat. The concave geometrical features were machined on the end surfaces of the other tool shoulders, which contained conical concavity angles of 5° and 10°, respectively. That is to say, three types of SCAs, i.e., 0°, 5°, and 10°, were designed to investigate the impact of SCA on the performances of the NTT-FSW joints. The scrolls were machined on all the shoulder end surfaces to develop an inwardly directed traction force under tool shoulder during NTT-FSW. All the shoulders had a same diameter of 26 mm. The conical tool pins with the same taper angles of 15° and right-hand threads were attached to all the shoulders for counterclockwise rotation. The pin length for all the tools was 7.8 mm. Figure 1 shows the schematic diagrams of the welding tools; note that the tools with SCAs of 0°, 5°, and 10° were abbreviated as 0-, 5-, and 10-tool, respectively.

The bead-on-plate NTT-FSW experiments, during which the tool tilting angle was set to 0°, were conducted along the longitudinal direction (perpendicular to the rolling direction) of the welding samples using an FSW machine. The rotation speed and welding speed of the tools were fixed at 600 rpm and 100 mm/min, respectively. A shoulder plunge depth of 0 mm was applied to all the tools to highlight the thermo-mechanical effects of SCA on the NTT-FSW. For the convenience of statement, the welds (or joints) produced by the tools with different SCAs were defined as 0-, 5-, and 10-welds (or joints), respectively. K-type thermocouples were utilized to measure the temperature of the samples during FSW. A dynamometer (K6D) was used for the measurement of welding forces during the welding. The dynamometer was located under welding fixture so that its axis Z was in the direction of tool axis.

After welding, the joints were all cross-sectioned perpendicular to the welding direction for metallographic analyses and mechanical tests. After successive steps of grinding and polishing, the samples were etched with Keller's reagent and observed by optical microscopy (OM, Olympus SZ61) and scanning electron microscope (SEM, Zeiss ULTRA 55) to evaluate the weld formation feature. The grain structures of the welds were determined by electron back-scattered diffraction (EBSD). The EBSD data was collected using a JEOL JSM-7001F SEM and processed with TSL OIM Analysis 6 software. Transmission electron microscopy (TEM, JEOL JEM 2100F) was used to investigate the sub-structures of the welds. The foil disk specimens for TEM were cut parallel to the welding direction and prepared through double jet electro-polishing using a solution of 30% nitric acid in methanol (18 V and − 35 °C). The TEM analyses were made at the {1 0 0} planes of the matrix.

The transverse tensile specimens were prepared with reference to China National Standard (GB/T2651-2008) (equivalent to American Standard ASTM B557-2). Tensile properties of each joint were evaluated using three tensile specimens cut from the same joint. The room temperature tensile test was carried out at a crosshead speed of 1 mm/min using an electron universal testing machine (Instron 5566). After tensile test, the SEM abovementioned (Zeiss ULTRA 55) was utilized to evaluate the fracture surface features. Microhardness was measured across the polished cross sections at a horizontal spacing of 1 mm and a vertical spacing of 1.3 mm. The testing load was 1.96 N for 10 s.

3 Results

3.1 Weld formation features

Figure 2 shows the cross sections of the joints formed at different SCAs. It should be noted that the retreating side (RS) is on the left and the advancing side (AS) is on the right for each

Table 1 Chemical compositions and mechanical properties of 5052-H32 aluminum alloy

Chemical compositions (wt%)								Mechanical properties	
Al	Mg	Si	Fe	Cr	Cu	Mn	Zn	Tensile strength	Elongation
Bal.	2.2~2.8	0.25	0.4	0.15~0.35	0.1	0.1	0.1	225 MPa	24%

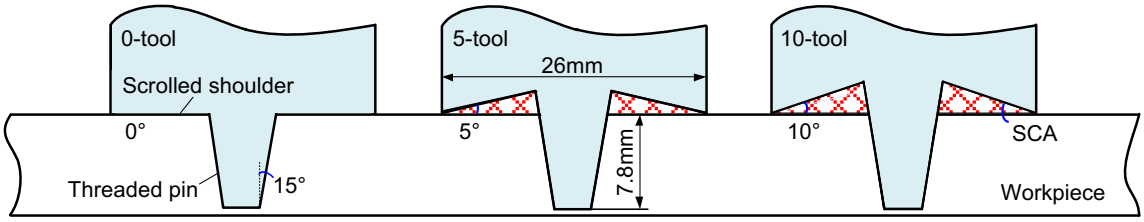

Fig. 1 Schematic diagrams of the welding tools

cross section in the figure; this convention is used throughout this manuscript. It can be seen that the SCA has significant influence on the nugget morphology, and two respects deserve attention. First, increase of SCA leads to a size decrease of the nugget zone. The nugget width was measured at the mid-thickness of each layer after equally dividing each joint into three layers from the top to bottom. The measurement result is displayed in Fig. 3. Obviously, the influence of SCA on nugget size is mainly concentrated in the upper part of weld where the nugget width decreases significantly with increasing SCA. This indicates that the material flow around the tool, especially that at the weld upper part, can be largely restricted as the SCA increases. Second, the band structure is observed in all the three nuggets. In the Nunes kinematic model, the band structure was claimed to be resulted from the superposition of the circular material flow around the pin with the downward material flow driven by the pin threads [11]. The large-SCA tools yield the band structures with smaller width at each layer, further demonstrating the control of the material plastic flow at large SCAs.

Since the tool pins used for the three tools had the same lengths and geometrical configurations, the different nugget morphologies are believed to be mainly resulted from the different shoulder-driven flows at various SCAs. The shoulder-driven flow level is determined by the interaction extent between shoulder end surface and the plastic material beneath tool shoulder. For the present study, the shoulder itself exerts a weak stirring effect to the workpiece due to the small shoulder penetration during the welding. However, a portion of the pin-sheared material can be extruded upwardly to the scrolls and concavity of shoulder [12, 13]. The shoulder then renders the forging force on the displaced material from the pin. For a fixed tool position relative to the workpiece, the large SCA serves as a large escape volume for the pin-sheared material, which should induce the relatively weak shoulder forging action. This assumption is verified by the load measurement results, as shown in Fig. 4. It is observed that the axial forces at the 0° and 5° SCAs are about 17.2 and 14.5 kN respectively at the start of the welding processes and then show the gradual decrease trends as the tools advance due to the heat accumulation in the welding. By contrast, the axial force is relatively low (~9.8 kN) at the 10° SCA and keeps a more stable state during FSW. The decrease of axial load limits both the horizontal and vertical material flows around the tool [14, 15], which should be responsible for the small nugget sizes and weak band structures at higher SCAs.

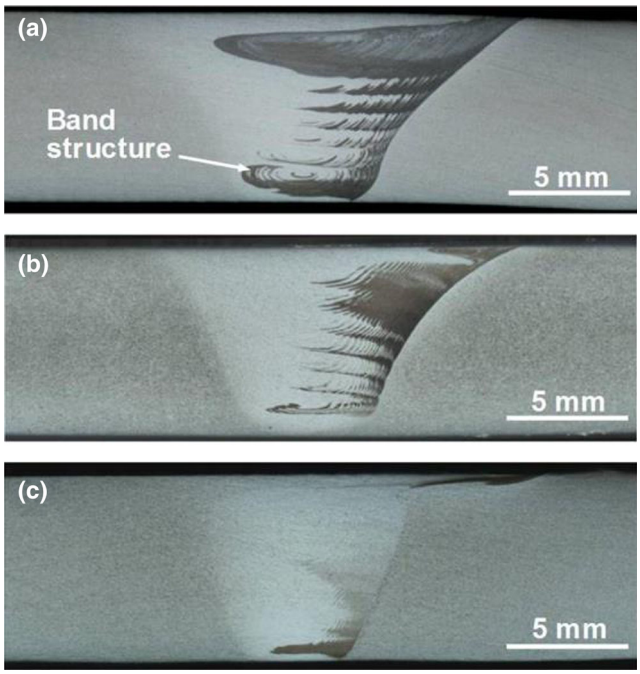

Fig. 2 Cross sections of **a** 0-joint, **b** 5-joint, and **c** 10-joint

3.2 Joint mechanical behavior

Table 2 shows the tensile properties of the NTT-FSW joints. The tensile strength is significantly increased with increasing the SCA from 0° to 5°. However, when a 10° SCA is reached, the joint strength is then again reduced from 218.0 MPa at 5°

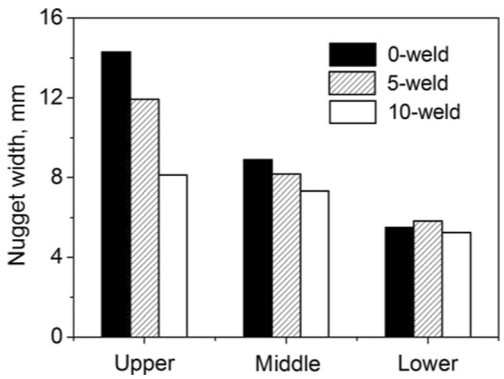

Fig. 3 Nugget widths of different layers of the joints

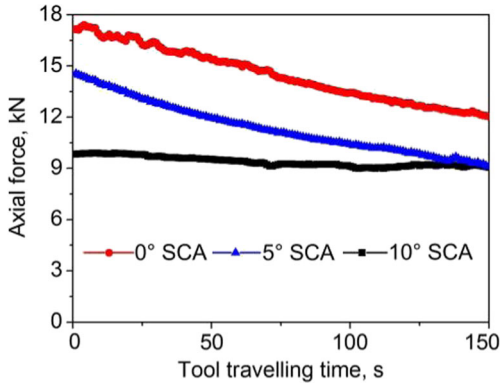

Fig. 4 Axial forces measured at different SCAs during the tool traveling

SCA to 196.4 MPa. These results imply that increasing the SCA from 0° to a certain value has positive effect on the strength improvement; however, if the SCA is increased above a certain level, a drop of the tensile properties of NTT-FSW joint may be attained. In the conventional FSW of 1.5-mm-thick 6082 aluminum alloy, higher joint strength was also obtained by using a concave-shouldered tool relative to that acquired by the flat shouldered tool [8]. However, the negative effect of larger SCA on joint properties has never been reported in previous studies on conventional FSW. The ductility follows different evolving trend with SCA from the tensile strength. The 5- and 10-joints exhibit similar elongations, higher than that of the 0-joint.

Figure 5 shows the fracture locations of the joints. The weld surfaces are at the top while the weld cross sections are at the bottom of the figure. The 0- and 5-joints are both fractured through the HAZs in the weld tracks during tensile test, and the fracture paths exhibit nearly 45° towards the tensile direction. The 10-joint also fails in the HAZ but the exact fracture location is outside the weld track. The fracture surfaces, extracted from the middle parts of the fracture paths, were also analyzed to further clarify the fracture features of joints (see Fig. 6). The shallow dimple feature of 0-joint is in accordance with its poor tensile elongation (see Fig. 6a). For the 5- and 10-joints, deep dimples with thick tearing edges full of micropores are observed in the fracture surfaces (see Fig. 6b, c), suggesting the higher plastic deformation levels during tensile test.

Table 2 Tensile properties of the joints formed at different SCAs

SCA	Tensile strength (MPa)/elongation (%)			
	Sample 1	Sample 2	Sample 3	Average
0°	202.6/17.8	204.3/19.1	200.5/18.1	202.4/18.3
5°	216.8/23.7	218.4/24.8	218.8/24.3	218.0/24.3
10°	196.2/24.7	196.6/24.5	196.6/24.2	196.4/24.4

The microhardness maps were measured across the two-dimensional cross sections in order to fully reveal the correlation between SCA and local mechanical characteristics of NTT-FSW joints, as shown in Fig. 7. The hardness of BM varies in the range of 62–70 Hv. By contrast, the hardness within the weld area exhibits a decrease for all the three joints. During the FSW of cold-worked aluminum alloys, the welding heat enables annealing and recovery to take place, and hence induces the formation of softening region with lower hardness than BM [16–18]. Since some strength recovery has occurred in the nugget zone and thermo-mechanically affected zone due to the grain refinement strengthening and strain strengthening effects, as commonly confirmed in the FSW of other non-heat treatable aluminum alloys [2, 6, 9], the joints all have the lowest hardness zones at the HAZs. The lowest hardness zones of 0- and 5-joints are located at the HAZ adjacent to pin periphery, while that of the 10-joint is moved outward to a further location from the weld center. Increase of SCA from 0° to 5° narrows the softening region and improves the hardness minimum; nevertheless, further increase of SCA to 10° considerably enlarges the softening region width and lowers the minimum hardness value.

The tensile properties are largely consistent with the hardness distributions. First, it is clear that the joints all fail in their lowest hardness locations during tensile test and the joints with larger hardness minima also exhibit superior tensile strengths, indicating that the integral tensile strength of the joint is actually determined by the hardness minimum. Second, the hardness profile also affects the joint ductility. Of interest is that the elongation of 10-joint is comparable with that of 5-joint although the former shows poor tensile strength. This should be attributed to the fact that the 10-joint has a large softening region width. During tensile test, the plastic deformation is primarily concentrated in the softening region [19, 20]. Larger amount of grains of 10-joint are able to be involved in the plastic deformation during tensile test, which retards the occurrence of work hardening and thus leads to the good ductility.

3.3 Microstructure evolution

The mechanical behavior of the FSW joints is essentially dependent on the microstructure evolution during the welding. Figures 8 and 9 show the microstructures extracted from the BM and the HAZs at the mid-thickness of joints on the AS. Note that for each joint, the HAZ position where the microstructure analysis was made is consistent with the minimum hardness location, which was 9, 8, and 16 mm from the weld center for the 0-, 5-, and 10-joints, respectively.

The BM exhibits coarse elongated grains (40.3 ± 8.7 μm in size) parallel to the rolling direction due to the work hardening (see Fig. 8a). The grain sizes of the HAZs are 44.3 ± 9.4, 41.8 ± 7.7, and 49.2 ± 11.3 μm for the 0-, 5-, and 10-welds,

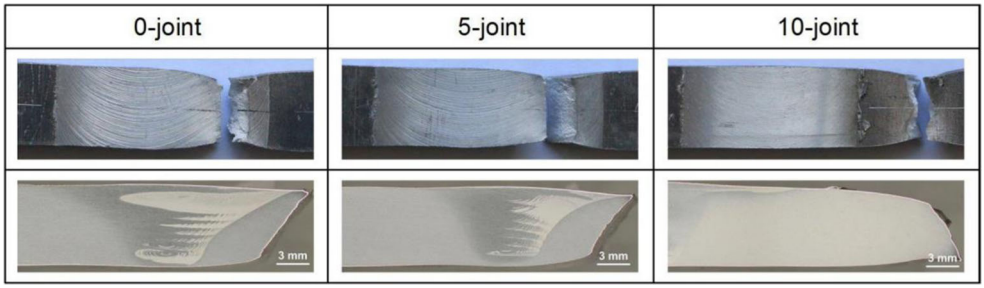

Fig. 5 Fracture locations of the joints

respectively (see Fig. 8b–d). Obviously, grain coarsening has occurred in all the HAZs during FSW, and the coarsening level is the lowest in the 5-joint and the highest in the 10-joint.

TEM micrographs of the BM and HAZs are shown in Fig. 9. It is clear that all the pictures contain a certain amount of dislocations, but they show different dislocation densities. Dislocation density was measured from the TEM micrographs following the usual procedure: A grid consisting of four horizontal and four vertical lines was superimposed on the central micro grain. The numbers n_h and n_v of intersections of dislocations with the horizontal and vertical grid lines were counted. Considering the total lengths of the horizontal (L_h) and vertical test lines (L_v), the dislocation density was acquired as the following [21]:

$$\rho = \frac{1}{t}\left(\frac{\sum n_v}{\sum L_v} + \frac{\sum n_h}{\sum L_h}\right) \quad (1)$$

Here, the thickness values of the specimen t, 120~175 nm, were evaluated from thickness fringes that appeared at high-angle grain boundaries under two-beam conditions.

Three dislocation density measurements were conducted for each type of the micrograph shown in Fig. 9. Considering the mean deviation from the three measurements, the dislocation densities of the BM, the 0-weld, 5-weld, and 10-weld are $(9.4 \pm 1.4) \times 10^{13}$ m^{-2}, $(5.3 \pm 1.8) \times 10^{13}$ m^{-2}, $(6.5 \pm 2.2) \times 10^{13}$ m^{-2}, and $(0.72 \pm 0.25) \times 10^{13}$ m^{-2}, respectively. Evidently, compared with the BM, the HAZs of 0- and 5-joints exhibit a lowering of dislocation densities. For a larger SCA of 10°, the dislocation density is dramatically decreased in the HAZ.

It is also observed from Fig. 9 that some second-phase particles are distributed in the BM and HAZs. For each TEM sample, the particle size was repeatedly measured for five times from different locations to attain an average size of second-phase particles. The BM has an average particle size of 141.6 ± 47.1 nm. In comparision, the HAZs of 0- and 5- joints are characterized by a coarsening of second-phase particles, whose particle sizes are 203.4 ± 36.3 and 158.8 ± 48.7 nm, respectively. The second-phase particles in the HAZ of 10-joint exhibit smaller size and rather low distribution density (see Fig. 9d), illustrating a significant particle dissolution during FSW.

In a word, microstructure deterioration in the HAZ, including the grain coarsening, the drop of dislocation density, and the coarsening/dissolution of second-phase particles, leads to the low mechanical properties of HAZ relative to the BM. It is found that the microstructure deterioration can be retarded by increasing the SCA from 0° to 5°; however, the present study also confirms that if the SCA reaches a certain level (10°), the microstructure deterioration may become worse, which induces inferior joint properties.

Tensile test results show that the weakest locations of the joints are all lying in the HAZ, that is to say, the welding thermal cycle is the dominant factor that determines the microstructure evolution and the resulting mechanical behavior of the weakest locations. Figure 10 plots the welding thermal cycles measured at the HAZs of the joints where the microstructure analyses were made. It can be seen that the 5-weld possesses the lowest peak temperature and the shortest high temperature dwelling time above a given temperature. Comparatively, the 10-weld exerts stronger thermal effect to

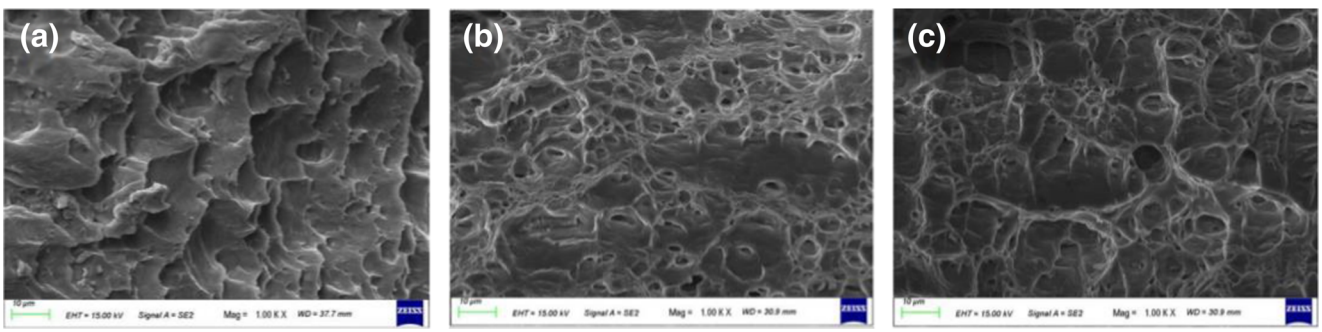

Fig. 6 Fracture surfaces of the failed joints: **a** 0-joint, **b** 5-joint, and **c** 10-joint

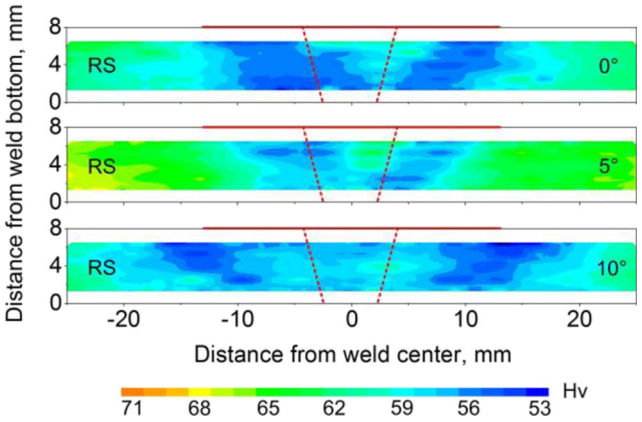

Fig. 7 Microhardness distributions of the joints formed at different SCAs. Note that the tool size is underlined by the red lines in the figure

the workpiece than the 0- and 5-welds. As far as the cold-worked aluminum alloys are concerned, the extent of annealing is primarily determined by welding thermal cycles. Thereby, it can be inferred that the welding thermal cycle is just the intrinsic reason for the structure-property evolution of NTT-FSW joint with the SCA.

4 Discussion

The above description suggests that the tool thermal effect as well as the structure-property of NTT-FSW joint is firstly improved and then deteriorated as the SCA increases from 0° to 10°. The pins used for the three types of tools are the same; therefore, the different thermal effects of the tools should be originated from the different shoulder geometries. The pin-sheared material is dragged into the bottom of shoulder due to the vertical material flow driven by the pin threads. The shoulder then exerts the thermo-mechanical effects to the workpiece through rendering a forging action on the displaced pin-sheared material. For a fixed tool plunge depth, the flat shoulder definitely exerts stronger interaction with the upward flow material than the concave shoulder because the shoulder end surface is closer to the workpiece top surface. This is just the reason why the 0-tool yields large axial force, strong thermal effect, and poor joint performances. Under the condition of 5° SCA, the position of shoulder end surface relative to workpiece top surface becomes larger in contrast to that of the flat shoulder. This not only weakens the interaction between shoulder end surface and the upward flow pin-sheared material, but also causes the frictional heat generated by tool shoulder to transfer a longer distance to the weld. These two factors together lead to the weakening of shoulder thermal effect during NTT-FSW and finally improve the structure-property of the joint. As expected, increase of the SCA from 5° to 10° leads to a further decrease in tool axial force. However, contrary to what one might suppose, the welding thermal cycle becomes stronger than that exerted by the 5-tool. This is surprising given that the heat generation is proportional to the axial force, as commonly observed in the conventional FSW of aluminum alloys [22, 23].

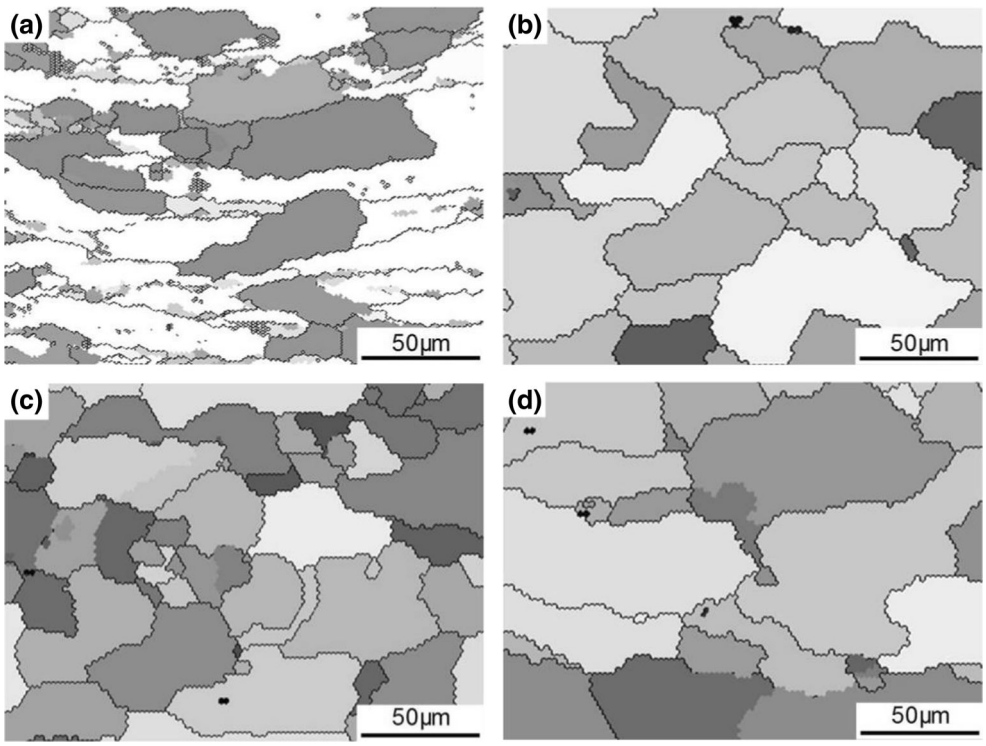

Fig. 8 Grain structures extracted from **a** the BM and **b**–**d** the HAZs of 0-, 5-, and 10-welds, respectively

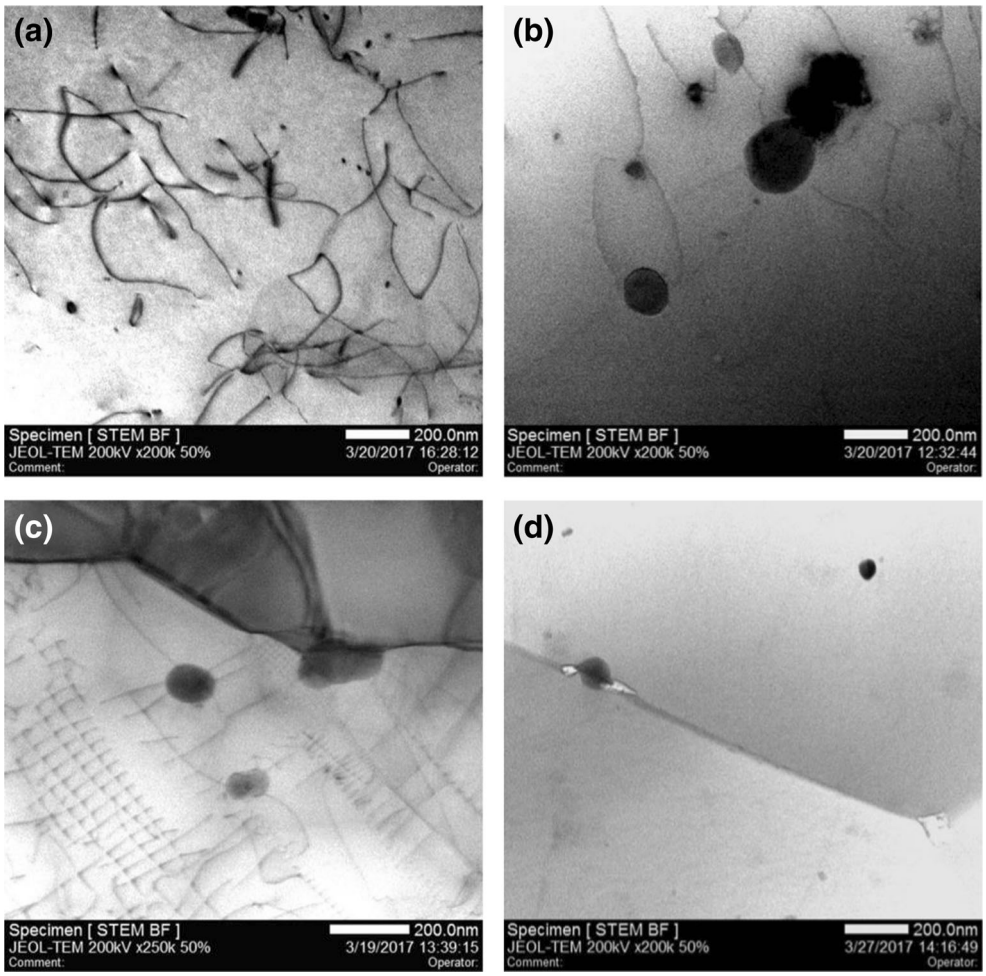

Fig. 9 TEM micrographs extracted from **a** the BM and **b**–**d** the HAZs of 0-, 5-, and 10-welds, respectively

The affecting characteristic of SCA on NTT-FSW can be further reflected by the morphology of shoulder-affected zone at the keyhole, as shown in Fig. 11. For the 0-weld, a complete shoulder-affected zone whose size is comparable with the shoulder diameter is lying around the keyhole (see Fig. 11a). The integrity of shoulder-affected zone around the keyhole is progressively reduced with increasing the SCA (see Fig. 11b, c), implying the weakening of shoulder-driven flow at higher SCAs. For a fixed shoulder diameter, the large SCA also results in the large area of shoulder end surface. However, the shoulder-affected zone around the keyhole indicates that the 10° concavity shoulder had the smallest contact area with the plastic material during FSW. It is interesting that how the largest extent of shoulder thermal effect can be produced under the conditions of the smallest contact area and the lowest axial force. In order to clarify the specificity of heat generation at the 10° SCA, the keyhole of 10-joint is cross-sectioned perpendicular to the welding direction and then investigated in detail. A distinct crack is observed at the discontinuous shoulder-driven flow region, which appears to be the interface between the shoulder-driven flow and the pin-driven flow (see Fig. 12a). Similarly, a continuously distributed crack is present on the cross section of the keyhole at the RS (see Fig. 12b, c, e). This is also observed at the AS until the outside edge of the shoulder-affected zone (see Fig. 12b, d, f, g). The tools all stay for 1 s before their extraction from the workpiece. That is to say, after the repeated tool rotation for 1 s, the shoulder-driven material (SDM) still shows an interface towards the BM. During this process, in addition to the heat generated by the shoulder end surface, the occurrence of the crack at the SDM/BM interface confirms that a secondary

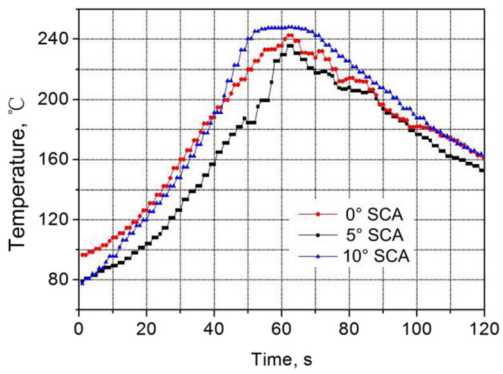

Fig. 10 Welding thermal cycles of the HAZs formed at different SCAs

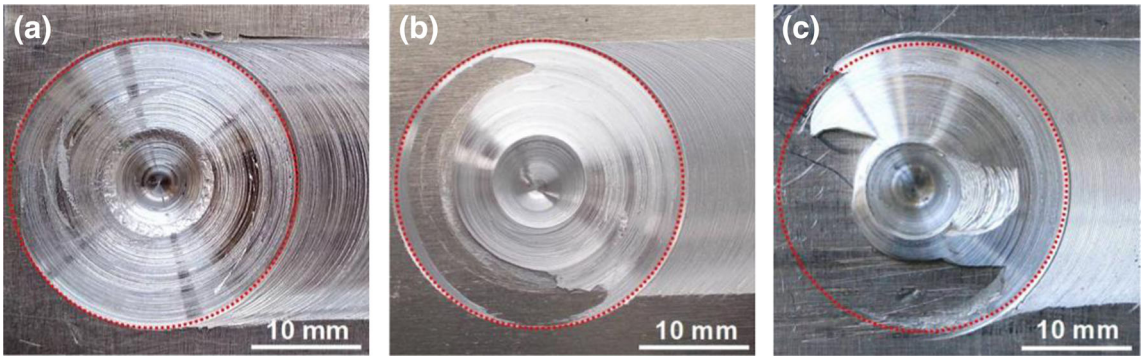

Fig. 11 Shoulder-affected zones around the keyholes of **a** 0-joint, **b** 5-joint, and **c** 10-joint. Note that the shoulder diameter is overlaid in the figure by red circles

sliding frictional heat should be simultaneously generated by the relative movement between the SDM and the BM. This is just the reason why the 10° concavity shoulder can yield stronger heat input even under the conditions of the lower tool axial force and smaller contact area with plastic material.

During NTT-FSW, the SDM hidden in the concave shoulder is mainly from the pin-sheared material, and thus it has an original interface towards the workpiece top surface (see Fig. 13a). Under such a case, the lower tool axial force and the large SCA both contribute to the generation of secondary frictional heat at the SCA of 10°. On the one hand, the SDM exerts lower extent of shearing effect to the top surface of BM due to the low tool axial force; on the other hand, the large SCA provides a large volume for the rapid flow of SDM. These two factors lead to the occurrences of the relative sliding movement between SDM and BM and consequently the generation of the secondary sliding frictional heat (see Fig. 13b). In comparison, the crack is not observed in the shoulder-affected zone around

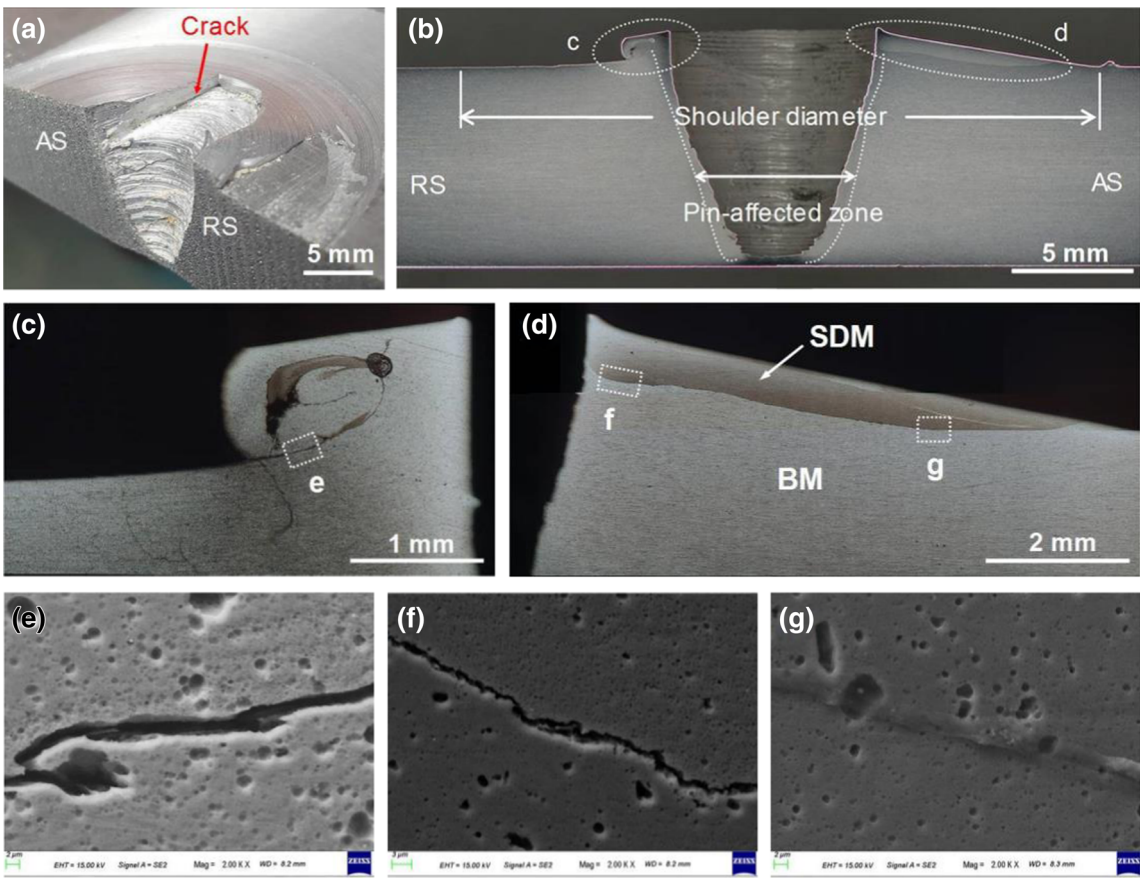

Fig. 12 Features of the keyhole formed by the 10-tool. **a** Crack between SDM and pin-driven material. **b** Cross section of the keyhole. **c**, **d** Enlarged views of the c and d locations marked in **b**. **e**–**g** Enlarged views of the e, f and g locations marked in **c** and **d**

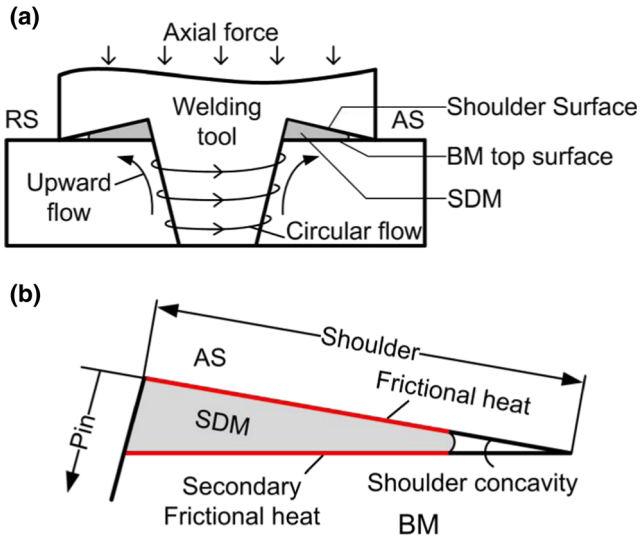

Fig. 13 Formation mechanisms of the secondary sliding frictional heat. **a** Material flow pattern during NTT-FSW. **b** Schematic view of the heat generation for the large SCA

the keyhole at the SCA of 5°. Under the conditions of the high tool axial force and the small SCA, the strong interaction occurs at the SDM/BM interface, and then the SDM together with the deformed BM is regulated as a laminar flow pattern by the shoulder-shearing effect. Because of this, the secondary sliding frictional heat generation is avoided and the heat input into the workpiece is relatively low. Similarly, although the concave-shouldered tool is also used in conventional FSW, the SDM beneath tool shoulder generally renders severe stirring action to the BM due to the existence of tool tilting angle, and thus the secondary sliding frictional heat generation occurring in the study is rarely observed in conventional FSW.

Above all, the shoulder exerts rather complex thermo-mechanical effects to the workpiece during NTT-FSW compared with the conventional FSW. Indeed, improving the SCA to a certain value leads to a relatively weak interaction between the shoulder and the BM, which is beneficial for the controlling of welding thermal cycles and the improvement of joint performances. Nevertheless, when the SCA is increased to a certain high level, the induced low tool axial force together with the large SCA causes the generation of secondary sliding frictional heat at the SDM/BM interface, because of this, the shoulder thermal effect can be inversely enhanced, resulting in the inferior joint properties. Therefore, the SCA is an important factor that requires careful optimization for NTT-FSW.

5 Conclusions

In this paper, the impact of SCA on the NTT-FSW of 5052 aluminum alloy has been investigated in detail. The conclusions of significance are drawn as follows:

(1) Attributed to the lowering of tool axial force, increase of SCA from 0° to 10° decreases the nugget width and reduces the band structure in the nugget, which is more significant at the weld upper part.
(2) A lowering of shoulder thermal effect from 0° to 5° SCA occurs due to the decrease of tool axial force, leading to an improvement of the structure-property of the NTT-FSW joint.
(3) With further increasing the SCA to 10°, the larger SCA and the lower tool axial force together cause the occurrence of the secondary sliding frictional heat at the SDM/BM interface, which enhances the shoulder thermal effect, deteriorates the microstructure evolution and degrades the mechanical properties of NTT-FSW joint.

Funding information This study was supported by National Natural Science Foundation of China (Grant No. 51505471) and Youth Innovation Promotion Association, Chinese Academy of Sciences (Grant No. 2015162).

References

1. Threadgill PL, Leonard AJ, Shercliff HR, Withers PJ (2009) Friction stir welding of aluminium alloys. Int Mater Rev 54:49–93
2. Cam G, Mistikoglu S (2014) Recent developments in friction stir welding of al-alloys. J Mater Eng Perform 23:1936–1953
3. Dubourg L, Dacheux P (2006) Design and properties of FSW tools: a literature review. 6th International Symposium on Friction Stir Welding, Session 1, Nr Montrral, Canada
4. Zhang YN, Cao X, Larose S, Wanjara P (2012) Review of tools for friction stir welding and processing. Can Metall Q 51:250–261
5. Hirano S, Okamoto K, Aota K, Okamura H, Aono Y, Odakura T (2001) Development of 3 dimensional type friction stir welding equipment. 3rd International Symposium on Friction Stir Welding, Session 1, Kobe, Japan
6. Amini S, Amiri MR, Barani A (2015) Investigation of the effect of tool geometry on friction stir welding of 5083-O aluminum alloy. Int J Adv Manuf Technol 76:255–261
7. Leal RM, Sakharova N, Vilaca P, Rodrigues DM, Loureiro A (2011) Effect of shoulder cavity and welding parameters on friction stir welding of thin copper sheets. Sci Technol Weld Join 16:146–152
8. Scialpi A, De Filippis LAC, Cavaliere P (2007) Influence of shoulder geometry on microstructure and mechanical properties of friction stir welded 6082 aluminium alloy. Mater Des 28:1124–1129
9. Zhang HJ, Wang M, Zhu Z, Zhang X, Yu T, Yang GX (2016) Improving the structure-property of aluminum alloy friction stir weld by using a non-shoulder-plunge welding tool. Int J Adv Manuf Technol 87:1095–1104
10. Longhurst WR, Strauss AM, Cook GE, Fleming PA (2010) Torque control of friction stir welding for manufacturing and automation. Int J Adv Manuf Technol 51:905–913
11. Schneider J, Beshears R, Nunes AC (2006) Interfacial sticking and slipping in the friction stir welding process. Mater Sci Eng A 435:297–304
12. Kumar K, Kailas SV (2008) The role of friction stir welding tool on material flow and weld formation. Mater Sci Eng A 485:367–374
13. Zhang HJ, Liu HJ (2012) Characteristics and formation mechanisms of welding defects in underwater friction stir welded aluminum alloy. Metall Microstr Anal 1:269–281

14. Arora A, Mehta M, De A, DebRoy T (2012) Load bearing capacity of tool pin during friction stir welding. Int J Adv Manuf Technol 61: 911–920
15. Forcellese A, Martarelli M, Simoncini M (2016) Effect of process parameters on vertical forces and temperatures developed during friction stir welding of magnesium alloys. Int J Adv Manuf Technol 85:595–604
16. Babu N, Karunakaran N, Balasubramanian V (2017) A study to estimate the tensile strength of friction stir welded AA 5059 aluminium alloy joints. Int J Adv Manuf Technol 93:1–9
17. Zhang ZH, Yang XQ, Zhang JL, Zhou G, Xu XD, Zou BL (2011) Effect of welding parameters on microstructure and mechanical properties of friction stir spot welded 5052 aluminum alloy. Mater Des 32:4461–4470
18. Hasan MM, Ishak M, Rejab MRM (2017) Influence of machine variables and tool profile on the tensile strength of dissimilar AA7075-AA6061 friction stir welds. Int J Adv Manuf Technol 90:2605–2615
19. Liu HJ, Fujii H, Maeda M, Nogi K (2003) Tensile properties and fracture locations of friction-stir-welded joints of 2017-T351 aluminum alloy. J Mater Process Technol 142:692–696
20. Zhang HJ, Liu HJ, Yu L (2011) Microstructural evolution and its effect on mechanical performance of joint in underwater friction stir welded 2219-T6 aluminium alloy. Sci Technol Weld Join 16:459–464
21. Pešička J, Kužel R, Dronhofer A, Eggeler G (2003) The evolution of dislocation density during heat treatment and creep of tempered martensite ferritic steels. Acta Mater 51:4847–4862
22. Schmidt H, Hattel J (2005) Modelling heat flow around tool probe in friction stir welding. Sci Technol Weld Join 10:176–186
23. Nandan R, Roy GG, Lienert TJ, Debroy T (2007) Three-dimensional heat and material flow during friction stir welding of mild steel. Acta Mater 55:883–895